INSTITUTE OF PHYSICS PUBLISHING JOURNAL OF PHYSICS: CONDENSED MATTER

J. Phys.: Condens. Matter **18** (2006) L259–L267 doi:10.1088/0953-8984/18/19/L05

LETTER TO THE EDITOR

Relationship of tunnelling magnetoresistance and buried-layer densities of states as derived from standing-wave excited photoemission

S-H Yang[1], B S Mun[2,3], N Mannella[2,3,6], A Nambu[2,7], B C Sell[2,4], S B Ritchey[2,4], F Salmassi[2], A Shick[5], S S P Parkin[1] and C S Fadley[2,4]

[1] IBM Almaden Research Center, San Jose, CA 95120, USA
[2] Materials Sciences Division, Lawrence Berkeley National Laboratory, Berkeley, CA 94720, USA
[3] Advanced Light Source, Lawrence Berkeley National Laboratory, Berkeley, CA 94720, USA
[4] Department of Physics, University of California at Davis, Davis, CA 95616, USA
[5] Institute of Physics, Czech Academy of Sciences, Prague, Czech Republic

Received 4 April 2006, in final form 12 April 2006
Published 27 April 2006
Online at stacks.iop.org/JPhysCM/18/L259

Abstract

We have measured the valence-band densities of states (DOSs) in buried CoFeB and CoFe layers in a magnetic tunnel junction using a novel extension of a recently developed standing wave/wedge soft x-ray photoemission technique. The CoFe DOS at the Fermi level is substantially enhanced when the CoFe thickness is reduced from 25 to 15 Å. This enhancement, which we suggest is due to the amorphous character of the CoFe when $\lesssim$20 Å in thickness and results in a spin-polarized peak in the DOS of primarily Co origin, can be directly correlated to marked improvements in magnetic transport and switching properties. This technique for studying buried-layer DOSs should also be applicable to other multilayer nanostructures.

(Some figures in this article are in colour only in the electronic version)

Magnetic tunnel junctions (MTJs) have received considerable attention due to promising applications as magnetic sensors, read heads, and magnetic random access memory (MRAM) [1]. While much effort has been focused on materials research so as to obtain higher tunnelling magnetoresistance (TMR), the physics of the magnetic tunnelling mechanism and how it is influenced by various materials choices is by no means fully understood. For example, Parkin *et al* [2] have recently found that inserting a thin $Co_{70}Fe_{30}$ layer (abbreviated hereafter as CoFe) of thickness $d_{CoFe} \lesssim 20$ Å between an amorphous insulating barrier of Al_2O_3 and an amorphous ferromagnetic (FM) layer of $Co_{56}Fe_{24}B_{20}$ (abbreviated CoFeB) yields substantially higher TMR values >60% at room temperature and tunnelling spin polarization

[6] Present address: Department of Physics, Stanford University, Stanford, CA 94305, USA.
[7] Present address: Chemistry Department, Brookhaven National Laboratory, Upton, NY 11973, USA.

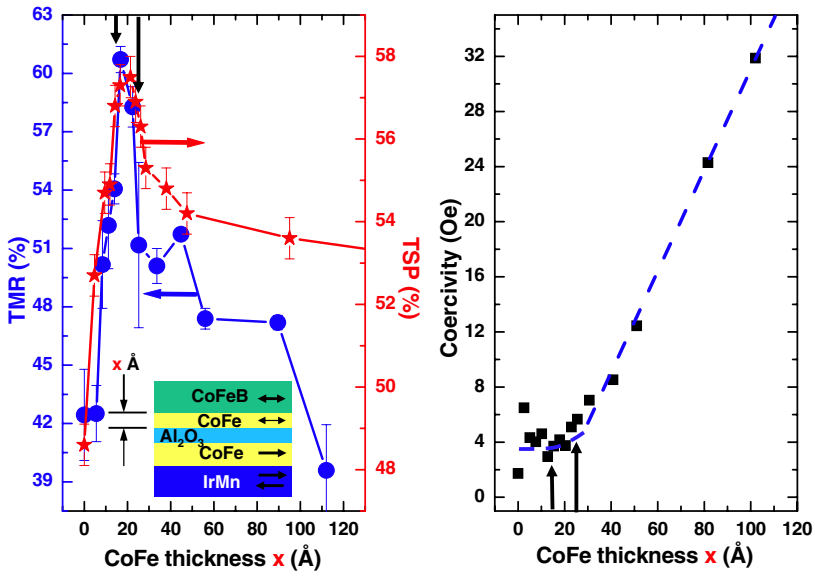

Figure 1. Summary of various transport-related measurements on a CoFeB|CoFe|Al_2O_3|CoFe|IrMn exchange-biased magnetic tunnel junction as a function of the thickness of the CoFe layer. (a) Spin polarization of tunnelling current and tunnel magnetoresistance. (b) Coercive field. The dashed line is hand drawn to guide the eye (from [2]). The black arrows indicate the CoFe layer thicknesses we have studied.

(TSP) magnitudes >55%, as compared to ∼40% and 45%, respectively, when the CoFe layer is not present. Some of their results are summarized in figure 1(a), where it is also clear that both TSP and TMR show a pronounced maximum at $d_{\mathrm{CoFe}} \approx 17$ Å, and a marked increase on decreasing d_{CoFe} from ∼25 to ∼17 Å. Coercivity results in figure 1(b) also show a steady decrease as d_{CoFe} is decreased from 100 to about 20 Å, dropping from about 32 to 4 Oe, and levelling off at the latter value for thicknesses below ∼20 Å. High-resolution cross-section TEM images also show that the CoFe layer is amorphous rather than polycrystalline when d_{CoFe} is less than ∼20 Å [2]. These results suggest that the onset of CoFe layer amorphization is responsible for the pronounced maximum in TSP and TMR. From Julliere's model [3], which predicts that TMR is determined by the spin-polarized DOSs in the FM layers at E_{F} via $\mathrm{TMR} = 2P_1P_2/[1 - P_1P_2]$, where P_1 and P_2 are the spin polarizations at E_{F} in the two FM layers of an MTJ, it is thus possible to suggest that the spin-polarized DOS at the Fermi level (E_{F}) in amorphous CoFe is significantly enhanced relative to that of crystalline CoFe. In order to test this last hypothesis and provide a more detailed understanding of these results in terms of electronic structure, we have extended a newly developed soft x-ray standing wave/wedge photoemission (PES) technique [4–6] so as to determine the DOSs in both the CoFeB and CoFe layers for two different values of $d_{\mathrm{CoFe}} = 15$ and 25 Å, that are very near to the peak in TMR in figure 1(a) and just above it, respectively. Our results show remarkable differences near E_{F} as d_{CoFe} varies across 20 Å, which can also be qualitatively linked via theory to an increase in the Co-derived spin-polarized DOS responsible for TSP and TMR.

Conventional PES cannot be simply applied to the measurement of the valence-band (VB) electronic structure of buried layers, since the VBs of all layers will be superimposed on one another in the low binding-energy region near E_{F} and the typical electron inelastic mean free paths (IMFPs) of ∼10–25 Å resulting from soft x-ray excitation [7] furthermore bias the spectra

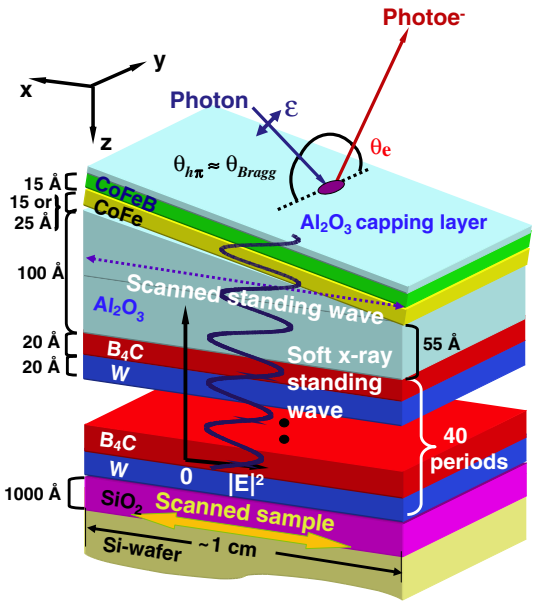

Figure 2. Experimental configuration and sample morphology used in the standing wave/wedge method.

to be much more sensitive to the surface layer(s). For the present case, it would thus be very difficult using conventional PES to separate out electrons emitted from the CoFe layer, as compared to those from the CoFeB layer. Adding a protective capping layer, a common procedure in such studies, would make this situation even worse. However, using a soft x-ray standing wave (SW) for excitation can directly yield depth-resolved information [4–6]. In this approach, the structures to be studied are grown on top of a synthetic multilayer mirror, including a wedge-shaped bottom layer, as shown in figure 2. Tuning the soft x-ray incidence angle to the Bragg condition $\theta_{\rm inc} = \theta_{\rm Bragg} \approx \sin^{-1}(\lambda_x/2d)$, with λ_x = the x-ray wavelength and d the period in the mirror, and then scanning the sample along the wedge direction then scans the SW of period d through buried layers. If the reflectivity of the multilayer is R, then the fractional modulation in the standing wave is given by $\sim \pm 2\sqrt{R}$: for a typical reflectivity of the multilayers we have used of 0.14, this yields ± 0.37, an effect large enough to strongly affect photoelectron intensities.

Here we apply this method to capped CoFeB/CoFe/Al_2O_3 trilayers, and demonstrate that, with the aid of x-ray optical (XRO) calculations described elsewhere [4, 6], it can be used to determine layer-specific VB spectra that are proportional to matrix-element-weighted DOSs, which can in turn be linked to TMR behaviour.

The soft x-ray mirror consisted of 40 bilayers composed of 20 Å of B_4C and 20 Å of W, with resulting periodicity $d = 40$ Å, and was grown on oxidized Si via rf magnetron sputtering. The following structure was grown on top of this mirror with dc magnetron sputtering: |Al_2O_3 protective cap-10 Å|CoFeB-15 Å|CoFe layer-15 Å or 25 Å|Al_2O_3 insulating barrier in wedge form—55–100 Å|, as shown in figure 2. PES measurements were performed at beamline 4.0.2 of the Advanced Light Source, which provides high brightness variable-polarization photons in the soft x-ray range (50–1500 eV). Linear p-polarized light (cf figure 2) with photon energy 1000 eV that is well away from any resonances in any element present in the sample was used, yielding $\theta_{\rm Bragg} = 9.3°$. The focused x-ray beam size is $\leqslant\sim 200$ μm and so much smaller than

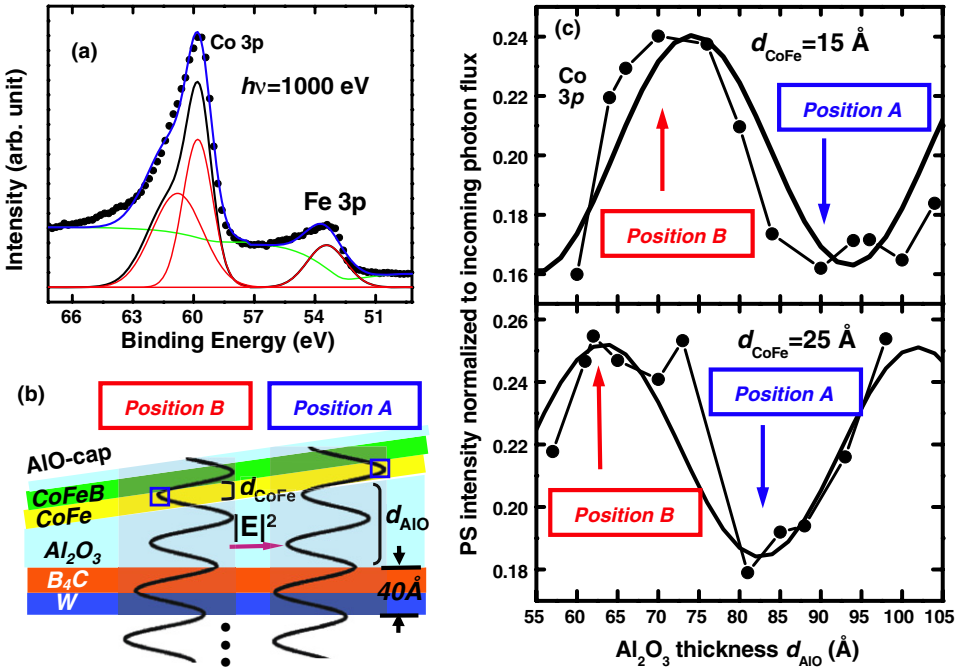

Figure 3. (a) Co and Fe 3p experimental spectra, obtained with a photon energy of 1000 eV, and including background subtraction and Gaussian fitting functions used to determine Co 3p intensities in (c). (b) Cross section view of $|\mathbf{E}|^2$ inside the multilayer + wedge sample, indicating special points at which the maximum (position A) and minimum (position B) of the SW are centred on the CoFe layer. (c) Plot of Co 3p intensity obtained from spectra like that in (a) versus insulating barrier thickness d_{AlO}, together with corresponding x-ray optical (XRO) calculations; the x-ray incidence angle is set in both at $\theta_{\mathrm{Bragg}} = 9.3°$.

the wedge length (∼1 cm), a necessary condition for employing the SW-wedge method [4]. Base pressures and energy resolutions were better than 7×10^{-11} Torr and 0.3 eV, respectively.

As a first step, core-level Al 2p, O 1s, and B 1s rocking curves were obtained by varying the x-ray incidence angle around θ_{Bragg} (data not shown here) and fitted to XRO calculations, thus giving estimates of interface diffusion/roughness lengths of $\sigma_{\mathrm{AlO-cap/CoFeB}} \approx 1.1$ Å, $\sigma_{\mathrm{CoFeB/CoFe}} \approx 2.3$ Å, and $\sigma_{\mathrm{CoFe/AlO-tunnel}} \approx 1.1$ Å. To determine the SW position most accurately, Co 3p intensities were measured as a function of sample x position, and thus also Al_2O_3 thickness d_{AlO} (cf figure 2). Co 3p is a shallow core level lying close to the VBs in kinetic energy ($E_{\mathrm{B}} \sim 60$ eV), so that the expected IMFP of ∼19 Å is very close to that of the VBs (∼20 Å). A Co 3p spectrum and its Fe 3p neighbour are shown in figure 3(a), together with background subtraction and Gaussian function fits. In figure 3(c), the total Co 3p intensities, as fitted to the two spin–orbit and multiplet-split components and measured at θ_{Bragg} by scanning the sample in x, are plotted together with XRO calculations as a function of d_{AlO}. Figure 3(b) illustrates the special SW positions A (maximum on CoFe) and B (minimum on CoFe) that are also indicated in figure 3(c). Experiment and theory are in very good agreement, with behaviour that has the expected 40 Å periodicity of the SW, maxima when the SW highlights the CoFeB layer, and a shift between the curves for the two thicknesses of about 8 Å that is consistent with the difference between d_{CoFeB} and d_{CoFe} of 10 Å and the different Co density in the layers.

We now consider VB PES spectra for these two samples and with various sample x positions, or equivalently various d_{AlO} (figures 4(a) and (b)). The spectra exhibit small, but

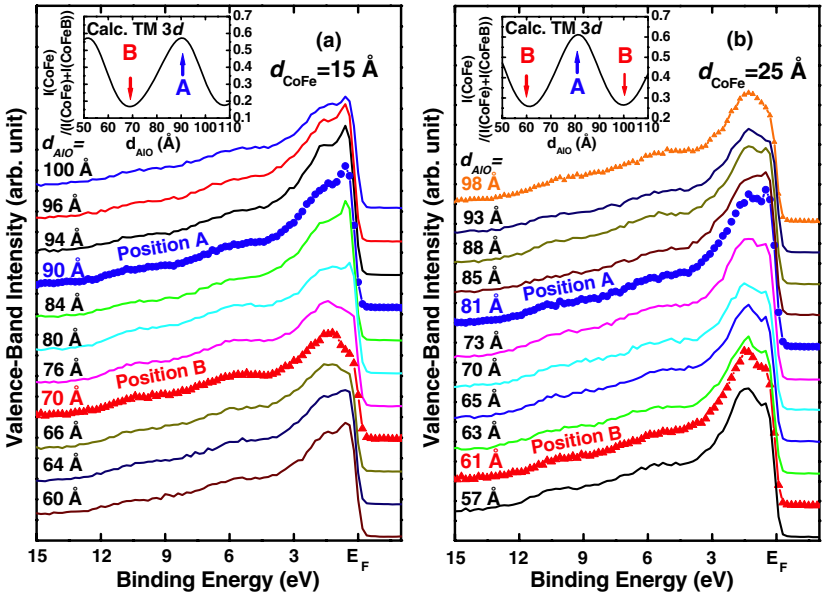

Figure 4. VB spectra obtained with a photon energy of 1000 eV and $\theta_{\mathrm{Bragg}} = 9.3°$, at various values of d_{AlO} and for two samples with (a) $d_{\mathrm{CoFe}} = 15$ Å and (b) $d_{\mathrm{CoFe}} = 15$ Å. Spectra obtained with the SW at positions A and B are highlighted. Insets show XRO calculations of $I(\mathrm{CoFe})/(I(\mathrm{CoFe}) + I(\mathrm{CoFeB}))$, with indications again of positions A and B.

easily observable, changes near E_{F} as the SW is swept through the CoFeB and CoFe layers, with the insulating capping layer not expected to produce significant intensity there due to the large ∼9 eV bandgap of Al_2O_3 [8]. We assign the various features in these spectra as follows: the weak feature at ∼10.5 eV to surface-layer adsorption of/reaction with residual gas, the broad peak at ∼4–6 eV peak mostly to O + Al bands in Al_2O_3 [8], and the double-peak structure+shoulder from ∼4 eV to E_{F} to the Co- and Fe-derived VBs [9]. Our 1000 eV photon energy strongly favours 3d emission relative to 4s emission from both Co and Fe by a factor of about 5–8 [10], and the 4s free-electron-like contributions to the DOS are also expected to be relatively featureless, so we will thus neglect them in the following analysis. Closer inspection of the spectra in figure 4 reveals that there is a peak nearest to E_{F} which varies systematically in intensity as the standing wave passes through the structure, with a maximum in relative intensity that occurs at position A, for which we calculate via XRO that the SW maximum sits on the CoFe layer, and a minimum in intensity when the SW minimum sits on the CoFe layer. Note further that this peak is much more enhanced for the 15 Å CoFe layer than for the 25 Å layer. The linkage of this behaviour to the CoFe layer is more quantitatively borne out by XRO simulations of the CoFe relative intensity, via the ratios of appropriate Fe 3d + Co 3d VB intensities, $I(\mathrm{CoFe})/[I(\mathrm{CoFeB}) + I(\mathrm{CoFe})]$, which are plotted versus d_{AlO} (or SW position) in the insets of figures 4(a) and (b). Via similar explanations to those used for Co 3p above, the extrema in this calculated ratio (e.g. a minimum at $d_{\mathrm{AlO}} = 70$ Å and maximum at 90 Å for $d_{\mathrm{CoFe}} = 15$ Å) occur prior to those of Co 3p by about 5 Å, and for $d_{\mathrm{CoFe}} = 25$ Å they occur at $d_{\mathrm{AlO}} = 60$ Å (minimum) and 80 Å (maximum), differing from those for $d_{\mathrm{CoFe}} = 15$ Å by 10 Å. This is as expected, since the SW period is equal to the bilayer thickness $d = 40$ Å when the radiation is incident at the Bragg angle θ_{Bragg}, with this providing the direct-space nature of the SW/wedge method [4–6].

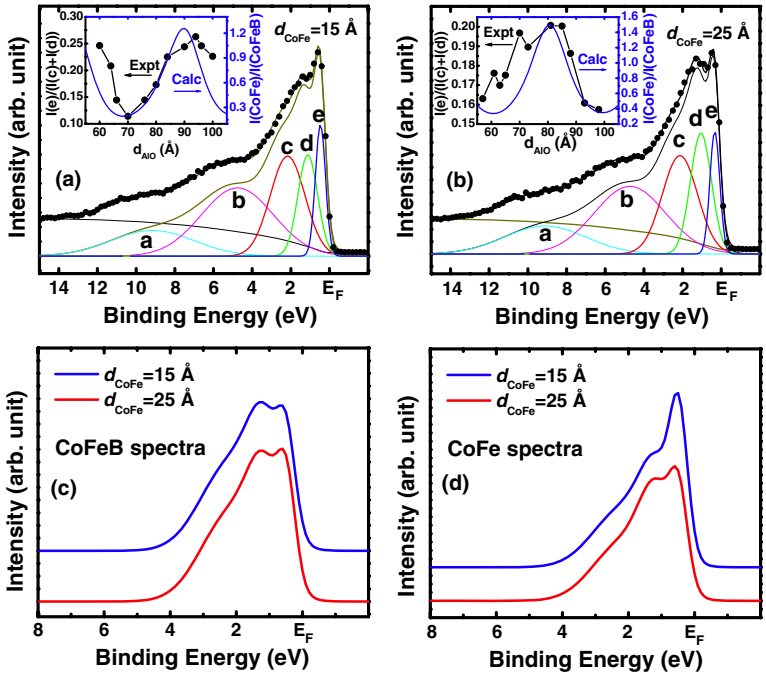

Figure 5. VB spectra at position A for (a) $d_{\mathrm{CoFe}} = 15$ Å and (b) $d_{\mathrm{CoFe}} = 25$ Å, together with background subtraction and five Gaussian functions ((a)–(e)) used to fit such spectra. The spectra are normalized at peak c. Insets show the experimental peak intensity ratio $I(e)/[I(c) + I(d)]$ and the XRO-calculated curve of $I(\mathrm{CoFe})/I(\mathrm{CoFeB})$. Layer-specific DOS spectra derived from the data of figure 5 via equation (5) are shown in (c) for CoFeB and in (d) CoFe for both values of d_{CoFe}.

To investigate the VB behaviour more quantitatively, the spectra have been fitted with five Gaussian peaks, as shown in figures 5(a) and (b), and labelled (a)–(e), with the Co 3d + Fe 3d-dominated spectral features near E_{F} being represented by the three peaks labelled c, d, and e. As a first observation, the ratio, $I(e)/[I(c) + I(d)]$ is found to be larger for $d_{\mathrm{Co\ Fe}} = 15$ Å than for 25 Å. This implies a significant difference in the electronic structures of these two layers. The insets in figures 5(a) and (b) further show plots of these experimental intensity ratios compared to XRO calculations of Co3d + Fe 3d intensity ratios that are obtained from weighted sums over each layer, $I(\mathrm{CoFe})/I(\mathrm{CoFeB})$, as a function of d_{AlO}. A comparison of the two curves in each inset in shows good qualitative agreement, especially as to the maxima in the relative intensity of peak e and the maximum calculated contribution from the CoFe layer.

Going beyond this to extract the layer-specific CoFe and CoFeB contributions for each d_{CoFe}, we have first modelled the PES process to include XRO SW effects, as well as electron excitation (cross section and light polarization) and emission (inelastic attenuation) processes [4]. The end goal is to determine the intensity ratios relating peaks d and e to peak c for each layer, assuming for simplicity that each layer is homogeneous, and then use these to synthesize the basic matrix-element-weighted DOS spectra from each layer. Supporting this assumption of layer homogeneity are TEM images for various thicknesses of the CoFe layer (not shown here). The two *independent* ratios within each layer i = CoFe or CoFeB are thus defined as follows:

$$R^{d,c}_{(0)i} = I^{d}_{(0)i}/I^{c}_{(0)i} \qquad \text{and} \qquad R^{e,c}_{(0)i} = I^{e}_{(0)i}/I^{c}_{(0)i}, \tag{1}$$

with a third arbitrary normalization ratio as $R^{c,c}_{(0)i} \equiv 1.0$. These ratios are intrinsic properties of each layer, and are independent of d_{AlO}. The contribution to the intensity of a given peak $j = c, d$, or e in a spectrum from one of the two layers can furthermore be calculated from

$$\begin{aligned} I^j_i(d_{\mathrm{AlO}}) &= C R^{j,c}_{(0)i} \int_{\Delta z(i)} |\vec{E}(z, d_{\mathrm{AlO}})|^2 \left[\rho_{\mathrm{Co},i} \frac{\mathrm{d}\sigma_{\mathrm{Co\ 3d}}}{\mathrm{d}\Omega} + \rho_{\mathrm{Fe},i} \frac{\mathrm{d}\sigma_{\mathrm{Fe\ 3d}}}{\mathrm{d}\Omega} \right] \mathrm{e}^{-z/(\Lambda_e(E^j_{\mathrm{kin}})\sin\theta)}\, \mathrm{d}z \\ &= C R^{j,c}_{(0)i} \beta_i(d_{\mathrm{AlO}}) \end{aligned} \tag{2}$$

with C a constant; z the coordinate measured from the top surface of the sample; $|\vec{E}(z, d_{\mathrm{AlO}})|^2$ the electric field strength squared for a given z and d_{AlO}, calculated from XRO [4] and allowing for the scanning of the SW through the interface as d_{AlO} is varied; ρ the relevant atomic density in each layer; $\mathrm{d}\sigma/\mathrm{d}\Omega$ the appropriate 3d atomic subshell cross section; Λ_e the kinetic-energy-dependent IMFP; θ the electron emission angle relative to the surface; the integral taken over the range $\Delta z(i)$ associated with each layer; and an obvious definition of β, which is derived from theory. Because the electron kinetic energies in peaks c, d, and e are so close (spanning only ∼996–1000 eV), the integral has been replaced by a single $\beta_i(d_{\mathrm{AlO}})$ that is valid for all intensities within a given layer i. The relative contributions to the intensities of each peak from each layer as a function of d_{AlO} will thus be given by

$$\frac{I^j_{\mathrm{CoFeB}}(d_{\mathrm{AlO}})}{I^j_{\mathrm{CoFe}}(d_{\mathrm{AlO}})} = \frac{R^{j,c}_{(0)\mathrm{CoFeB}} \beta_{\mathrm{CoFeB}}(d_{\mathrm{AlO}})}{R^{j,c}_{(0)\mathrm{CoFe}} \beta_{\mathrm{CoFe}}(d_{\mathrm{AlO}})}. \tag{3}$$

The intensities of all three peaks in a given spectrum are obtained by summing over the contributions from the two layers as

$$\begin{aligned} I^c(d_{\mathrm{AlO}}) &= \left[1 + \frac{\beta_{\mathrm{CoFeB}}(d_{\mathrm{AlO}})}{\beta_{\mathrm{CoFe}}(d_{\mathrm{AlO}})} \right] I^c_{\mathrm{CoFe}}(d_{\mathrm{AlO}}) \\ I^d(d_{\mathrm{AlO}}) &= \left[1 + \frac{R^{d,c}_{(0)\mathrm{CoFeB}}}{R^{d,c}_{(0)\mathrm{CoFe}}} \frac{\beta_{\mathrm{CoFeB}}(d_{\mathrm{AlO}})}{\beta_{\mathrm{CoFe}}(d_{\mathrm{AlO}})} \right] R^{d,c}_{(0)\mathrm{CoFe}} I^c_{\mathrm{CoFe}}(d_{\mathrm{AlO}}) \\ I^e(d_{\mathrm{AlO}}) &= \left[1 + \frac{R^{e,c}_{(0)\mathrm{CoFeB}}}{R^{e,c}_{(0)\mathrm{CoFe}}} \frac{\beta_{\mathrm{CoFeB}}(d_{\mathrm{AlO}})}{\beta_{\mathrm{CoFe}}(d_{\mathrm{AlO}})} \right] R^{e,c}_{(0)\mathrm{CoFe}} I^c_{\mathrm{CoFe}}(d_{\mathrm{AlO}}). \end{aligned} \tag{4}$$

Rearranging, we arrive at equations for the two unique intensity ratios derived from fitting peaks to each experimental spectrum, which in turn involve only the four layer-specific intensity ratios of equation (1) as unknowns,

$$\begin{aligned} R^{d,c}(d_{\mathrm{AlO}}) &= I^d(d_{\mathrm{AlO}})/I^c(d_{\mathrm{AlO}}) \\ &= \left[R^{d,c}_{(0)\mathrm{CoFe}} + R^{d,c}_{(0)\mathrm{CoFeB}} \frac{\beta_{\mathrm{CoFeB}}(d_{\mathrm{AlO}})}{\beta_{\mathrm{CoFe}}(d_{\mathrm{AlO}})} \right] \Bigg/ \left[1 + \frac{\beta_{\mathrm{CoFeB}}(d_{\mathrm{AlO}})}{\beta_{\mathrm{CoFe}}(d_{\mathrm{AlO}})} \right] \\ R^{e,c}(d_{\mathrm{AlO}}) &= I^e(d_{\mathrm{AlO}})/I^c(d_{\mathrm{AlO}}) \\ &= \left[R^{e,c}_{(0)\mathrm{CoFe}} + R^{e,c}_{(0)\mathrm{CoFeB}} \frac{\beta_{\mathrm{CoFeB}}(d_{\mathrm{AlO}})}{\beta_{\mathrm{CoFe}}(d_{\mathrm{AlO}})} \right] \Bigg/ \left[1 + \frac{\beta_{\mathrm{CoFeB}}(d_{\mathrm{AlO}})}{\beta_{\mathrm{CoFe}}(d_{\mathrm{AlO}})} \right]. \end{aligned} \tag{5}$$

Finally, with $R^{d,c}(d_{\mathrm{AlO}})$ and $R^{e,c}(d_{\mathrm{AlO}})$ that are determined from fits to the experimental data and β values that are obtained from XRO calculations, we have evaluated equations (5) for all spectra (i.e. all values of d_{AlO}), and analysed the resulting overdetermined sets of simple linear equations via a least-squares fitting method to derive the four required ratios $R^{j,c}_{(0)i} = I^j_{(0)i}/I^c_{(0)i}$ ($j = d, e, i =$ CoFe, CoFeB) [11]. These ratios then permit synthesizing the basic 3d spectra for CoFeB and CoFe layers, as shown in figures 5(c) and (d).

It is first remarkable that the CoFeB spectra are very similar for both d_{CoFe} values. Thus, we conclude that the electronic structure of the CoFeB layer is independent of CoFe interface layer

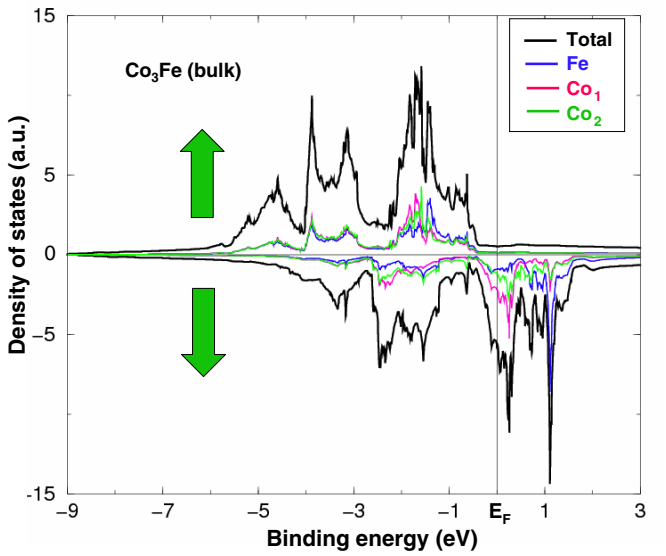

Figure 6. Spin-resolved density-of-states results from a local-density (FP-FLAPW) calculation for Co_3Fe in the Fe_3Al ordered structure, including a decomposition of these results into contributions from the Fe and the two structurally inequivalent types of Co atoms present (from [16]).

thickness over these values, as might be expected. By contrast, there is a marked difference in the CoFe spectra for the two d_{CoFe} values, with a much stronger peak near E_F for $d_{CoFe} = 15$ Å. These results thus provide a direct microscopic explanation, via the Julliere model, for the d_{CoFe} value at which both the TSP and TMR data in figure 1 exhibit maxima, provided that this peak is strongly spin-polarized.

A qualitative connection of these results with the amorphous character of the CoFe layer when $d_{CoFe} \leqslant \sim 20$ Å is also possible via theory. Considering first the influence of amorphization, we note that the DOS at E_F in a metal or a metal alloy is generally expected to be enhanced when it goes from a crystalline to an amorphous state due to a reduction of the average number of bonding interactions and/or of the integrated bond strength to each atom [12]. As a simplified justification of this expectation, the DOS at E_F decreases as atoms approach each other to make bonds, through the creation of bonding states at lower energies below E_F and anti-bonding states at higher energies above E_F, leading to a lower DOS at E_F. In fact, it has been argued that systems among a set with the minimum density of states at E_F will be the most stable [12]. This kind of bonding/anti-bonding reasoning has also been used previously to analyse the electronic structure of CoFe alloys [9]. Electronic structure calculations [13, 14] for Fe metal and its alloys further show that the DOS at E_F for amorphous Fe is substantially enhanced compared with bcc Fe. Crystalline Co_xFe_{1-x} is also known to have a bcc structure for $x < 0.85$ at RT, [15] and our 25 Å $Co_{70}Fe_{30}$ layer is thus probably bcc. Thus, we finally expect a higher density of states at E_F in the amorphous 15 Å $Co_{70}Fe_{30}$ layer as compared to the crystalline 25 Å layer.

As final theoretical input, we show in figure 6 some spin-resolved theoretical densities of states for an ordered Co_3Fe crystal in the Fe_3Al structure, as determined by the first-principles fully linearized augmented plane-wave (FP-FLAPW) method [16]. The spin-resolved DOS curves shown here agree excellently with an earlier calculation for Co_3Fe [9], with both sets of calculations indicating that the DOS peak near E_F is strongly minority spin polarized. Beyond

this, the atom-resolved contributions shown in figure 6 indicate that this peak is strongly Co 3d in character. Thus, although these calculations are not for the precise disordered alloy system being studied here, we can make a strong argument that the enhanced intensity for the 15 Å CoFe layer is in fact strongly spin polarized and largely of Co 3d character. Future SW/wedge studies using resonant PES would clarify the elemental origin of this enhanced DOS at E_F experimentally, and represent one very interesting direction for future studies. Adding electron spin resolution to such experiments is another obvious future direction, albeit one which is significantly more difficult due to the $\sim 10^3$–10^4 times longer data acquisition times with present spin detection systems. Beyond providing microscopic insight into the behaviour of the particular MTJ studied here, the extension of the standing wave/wedge method we have illustrated here should also be applicable to a wide variety of other magnetic and non-magnetic multilayer nanostructures.

This work was supported by the Director, Office of Science, Office of Basic Energy Sciences, Materials Science and Engineering Division, US Department of Energy, under contract No DE-AC03-76SF00098, and the IBM–Infineon Technologies joint MRAM research project. We are also grateful to E Arenholz and A Young for support in carrying out these experiments.

References

[1] Parkin S S P, Roche K P, Samant M G, Rice P M, Beyers R B, Scheuerlein R E, O'Sullivan E J, Brown S L, Bucchigano J, Abraham D W, Lu Yu, Rooks M, Trouilloud P L, Wanner R A and Gallagher W J 1999 *J. Appl. Phys.* **85** 5828

[2] Parkin S S P, Yang S-H, Hughes B, Samant M G and Chaiser K 2006 submitted (with partial results of this study shown in figure 1)

[3] Julliere M 1975 *Phys. Lett.* A **54** 225

[4] Yang S-H, Mun B S, Mannella N, Kim S-K, Kortright J B, Underwood J H, Salmassi F, Arenholz E, Young A, Hussain Z, Van Hove M A and Fadley C S 2002 *J. Phys.: Condens. Matter* **14** L1

[5] Yang S-H, Mun B S and Fadley C S 2004 *Synchrotron Radiat. News* **17** 24

[6] Fadley C S, Yang S-H, Mun B S and Garcia de Abajo J 2003 *Solid-State Photoemission and Related Methods: Theory and Experiment* ed W Schattke and M A Van Hove (Berlin: Wiley–VCH) (invited chapter)

[7] Tanuma S, Powell C J and Penn D R 1991 *Surf. Interface Anal.* **17** 911
Tanuma S, Powell C J and Penn D R 1993 *Surf. Interface Anal.* **21** 165
Jablonski A and Powell C J 1999 *J. Electron. Spectrosc.* **100** 137

[8] Mo S D and Ching W Y 1998 *Phys. Rev.* B **57** 15219

[9] Schwart K, Mohn P, Blaha P and Kübler J 1984 *J. Phys. F: Met. Phys.* **14** 2659

[10] Yeh J J and Lindau I 1985 *At. Data Nucl. Data Tables* **32** 1

[11] Mannella N, Marchesini S, Kay A W, Nambu A, Gresch T, Yang S-H, Mun B S, Rosenhahn A and Fadley C S 2004 *J. Electron Spectrosc. Relat. Phenom.* **141** 45–59 (see equations (5)–(10) and associated discussion, where the same mathematical procedure is used to correct for detector non-linearity)

[12] Moruzzi V L, Oelhafen P and Williams A R 1983 *Phys. Rev.* B **27** 7194

[13] Fujiwara T 1985 *Nippon Butshuri Gakkaishi* **40** 209

[14] Kakehashi Y 1993 *Phys. Rev.* B **47** 3185

[15] Abrikosov I A, James P, Eriksoon O, Söderlind P, Ruban A V, Skriver H L and Johannson B 1996 *Phys. Rev.* B **54** 3380

[16] Shick A, unpublished results